



HAL
open science

JWST MIRI Imager Observations of Supernova SN 1987A

P Bouchet, R Gastaud, A Coulais, M.J Barlow, C Fransson, P.J Kavanagh, J
Larsson, T Temim, O.C Jones, A.S Hirschauer, et al.

► **To cite this version:**

P Bouchet, R Gastaud, A Coulais, M.J Barlow, C Fransson, et al.. JWST MIRI Imager Observations of Supernova SN 1987A. *The Astrophysical Journal*, 2024, 965 (1), pp.51. 10.3847/1538-4357/ad2770 . hal-04503421

HAL Id: hal-04503421

<https://hal.science/hal-04503421>

Submitted on 20 Apr 2024

HAL is a multi-disciplinary open access archive for the deposit and dissemination of scientific research documents, whether they are published or not. The documents may come from teaching and research institutions in France or abroad, or from public or private research centers.

L'archive ouverte pluridisciplinaire **HAL**, est destinée au dépôt et à la diffusion de documents scientifiques de niveau recherche, publiés ou non, émanant des établissements d'enseignement et de recherche français ou étrangers, des laboratoires publics ou privés.



Distributed under a Creative Commons Attribution 4.0 International License



JWST MIRI Imager Observations of Supernova SN 1987A

P. Bouchet¹, R. Gastaud², A. Coulais^{1,3}, M. J. Barlow⁴, C. Fransson⁵, P. J. Kavanagh^{6,7}, J. Larsson⁸, T. Temim⁹, O. C. Jones¹⁰, A. S. Hirschauer¹¹, T. Tikkanen¹², J. A. D. L. Blommaert¹³, O. D. Fox¹¹, A. Glasse¹⁰, N. Habel¹⁴, J. Hjorth¹⁵, J. Jaspers^{6,7}, O. Krause¹⁶, R. M. Lau¹⁷, L. Lenkić¹⁴, M. Meixner¹⁸, O. Nayak¹¹, A. Rest^{11,19}, B. Sargent^{11,20}, R. Wesson²¹, G. S. Wright¹⁰, L. Colina²², E. F. van Dishoeck^{23,24}, M. Güdel^{25,26,27}, Th. Henning²³, P.-O. Lagage¹, G. Östlin⁵, T. P. Ray⁷, and B. Vandenbussche²⁸

¹ Université Paris-Saclay, Université Paris Cité, CEA, CNRS, AIM, F-91191 Gif-sur-Yvette, France; Patrice.Bouchet@cea.fr

² Université Paris-Saclay, CEA, DEDIP, 91191, Gif-sur-Yvette, France

³ LERMA, Observatoire de Paris, Université PSL, Sorbonne Université, CNRS, Paris, France

⁴ Department of Physics and Astronomy, University College London (UCL), Gower Street, London WC1E 6BT, UK

⁵ Department of Astronomy, Stockholm University, The Oskar Klein Centre, AlbaNova, SE-106 91 Stockholm, Sweden

⁶ Department of Experimental Physics, Maynooth University, Maynooth, Co. Kildare, Ireland

⁷ Dublin Institute for Advanced Studies, School of Cosmic Physics, Astronomy & Astrophysics Section, 31 Fitzwilliam Place, Dublin 2, Ireland

⁸ Department of Physics, KTH Royal Institute of Technology, The Oskar Klein Centre, AlbaNova, SE-106 91 Stockholm, Sweden

⁹ Department of Astrophysical Sciences, Princeton University, Princeton, NJ 08544, USA

¹⁰ UK Astronomy Technology Centre, Royal Observatory, Blackford Hill, Edinburgh, EH9 3HJ, UK

¹¹ Space Telescope Science Institute, 3700 San Martin Drive, Baltimore, MD 21218, USA

¹² School of Physics & Astronomy, Space Research Centre, University of Leicester, Space Park Leicester, 92 Corporation Road, Leicester LE4 5SP, UK

¹³ Astronomy and Astrophysics Research Group, Department of Physics and Astrophysics, Vrije Universiteit Brussel, Pleinlaan 2, B-1050 Brussels, Belgium

¹⁴ Stratospheric Observatory for Infrared Astronomy, NASA Ames Research Center, Mail Stop 204-14, Moffett Field, CA 94035, USA

¹⁵ DARK, Niels Bohr Institute, University of Copenhagen, Jagtvej 128, 2200 Copenhagen, Denmark

¹⁶ Max Planck Institute for Astronomy, Heidelberg (MPIA), Germany

¹⁷ NSF's NOIR Lab 950 N. Cherry Avenue, Tucson, AZ 85721, USA

¹⁸ Jet Propulsion Laboratory, California Institute of Technology, 4800 Oak Grove Dr., Pasadena, CA 91109, USA

¹⁹ Department of Physics and Astronomy, Johns Hopkins University, 3400 North Charles Street, Baltimore, MD 21218, USA

²⁰ Center for Astrophysical Sciences, The William H. Miller III Department of Physics and Astronomy, Johns Hopkins University, Baltimore, MD 21218, USA

²¹ School of Physics and Astronomy, Cardiff University, Queen's Buildings, The Parade, Cardiff, CF24 3AA, UK

²² Centro de Astrobiología (CAB), CSIC-INTA, Ctra. de Ajalvir km 4, Torrejón de Ardoz, E-28850, Madrid, Spain

²³ Max-Planck Institut für Extraterrestrische Physik (MPE), Giessenbachstr., 1, D-85748, Garching, Germany

²⁴ Leiden Observatory, Leiden University, 2300 RA Leiden, The Netherlands

²⁵ Dept. of Astrophysics, University of Vienna, Türkenschanzstr. 17, A-1180 Vienna, Austria

²⁶ Max-Planck-Institut für Astronomie (MPIA), Königstuhl, 17, D-69117 Heidelberg, Germany

²⁷ ETH Zürich, Institute for Particle Physics and Astrophysics, Wolfgang-Pauli Str., 27, 8093 Zürich, Switzerland

²⁸ Institute of Astronomy, KU Leuven, Celestijnenlaan 200D, 3001 Leuven, Belgium

Received 2023 December 22; revised 2024 February 6; accepted 2024 February 6; published 2024 April 4

Abstract

There exist very few mid-infrared (IR) observations of supernovae (SNe) in general. Therefore, SN 1987A, the closest visible SN in 400 yr, gives us the opportunity to explore the mid-IR properties of SNe, the dust in their ejecta, and the surrounding medium and to witness the birth of an SN remnant (SNR). The James Webb Space Telescope, with its high spatial resolution and extreme sensitivity, gives a new view on these issues. We report on the first imaging observations obtained with the Mid-InfraRed Instrument (MIRI). We build temperature maps and discuss the morphology of the nascent SNR. Our results show that the temperatures in the equatorial ring (ER) are quite nonuniform. This could be due to dust destruction in some parts of the ring, as had been assumed in some previous works. We show that the IR emission extends beyond the ER, illustrating the fact that the shock wave has now passed through this ring to affect the circumstellar medium on a larger scale. Finally, while submillimeter Atacama Large Millimeter Array observations have hinted at the location of the compact remnant of SN 1987A, we note that our MIRI data have found no such evidence.

Unified Astronomy Thesaurus concepts: Type II supernovae (1731); Core-collapse supernovae (304); Supernova remnants (1667)

1. Introduction

Our interpretation of the Universe is being transformed by the advent of the James Webb Space Telescope (JWST, Gardner et al. 2023).

Its unparalleled infrared (IR) sensitivity provides a revolutionary view into the properties and characteristics of a wide

range of astrophysical phenomena. During the first year of JWST operations, the iconic supernova SN 1987A, the closest optical SN in 400 yr (see McCray 1993; McCray & Fransson 2016 for reviews) was among the first targets selected for observation. Astronomers have followed its full evolution across the entire electromagnetic spectrum, owing to its close proximity to the nearby Large Magellanic Cloud (LMC), as it completes its transformation into an SN remnant (SNR).

The first possible spatially resolved detection of mid-IR emission for any SN was reported by Bouchet et al. (2004), using the Gemini South 8 m telescope at the position of SN

Original content from this work may be used under the terms of the [Creative Commons Attribution 4.0 licence](https://creativecommons.org/licenses/by/4.0/). Any further distribution of this work must maintain attribution to the author(s) and the title of the work, journal citation and DOI.

1987A on day 6067 since the explosion. Following that, Spitzer observations of SN 1987A spanned more than a decade. Since day ~ 4000 after outburst, its mid-IR emission has been dominated by dust, most probably from the equatorial ring (ER), rather than from the ejecta. Indeed, the ground-based images of Bouchet et al. (2004) showed this directly and were confirmed by the lower-resolution Spitzer images that required deconvolution (or modeling). Decomposition of the marginally resolved emission also confirms mid-IR domination by dust and shows that the west side has been brightening relative to the other portions of the ER (Bouchet & Danziger 2014).

From ~ 6000 to ~ 8000 days after the explosion, Spitzer observations included broadband photometry at 3.6–24 μm and low- and moderate-resolution spectroscopy at 5–35 μm (Arendt et al. 2016, 2020). After Spitzer’s helium cryogen was exhausted in 2009, however, only the IRAC 3.6 and 4.5 μm bands remained operational at the warmer spacecraft temperatures, restricting further IR observations to these imaging wavelengths alone. While the exact nature of the emission at these wavelengths has not been certain, regular observations of SN 1987A continued in order to monitor the evolution of the interaction of the blast wave with the ER and to develop a clear picture of the evolving relationship between the IR emission at these wavelengths and emission at optical and X-ray wavelengths (Dwek et al. 2008, 2010; Arendt et al. 2016). These data show that the 3.6 and 4.5 μm brightness had clearly begun to fade after day ~ 8500 , and no longer tracked the X-ray emission as well as it had at earlier epochs. This can be explained by the destruction of the dust in the ER on timescales shorter than the cooling time for the shocked gas. It was also found that the evolution of the late-time IR emission was similar to the fading optical emission at that epoch (see, for instance, Dwek et al. 2010).

Using the Gemini South 8 m telescope, high-resolution 11.7 and 18.3 μm mid-IR images of SN 1987A were also obtained at day 6526 (Bouchet et al. 2006). It was shown that most of the emission arising from the ER was thermal in origin from silicate dust, presumed to have condensed out in the red supergiant wind of the progenitor star. They estimated the dust temperature to be $\sim 166 \pm 15$ K.

Comparison of the Gemini 11.7 μm image with Chandra X-ray images, Hubble Space Telescope (HST) UV–optical (UVO) images, and Australia Telescope Compact Array (ATCA) radio synchrotron images shows generally good correlation across all wavelengths. If the dust resides in the diffuse X-ray emitting gas then it is collisionally heated. The IR emission can then be used to derive the plasma temperature and density, which were found to be in good agreement with those inferred from the X-rays (Dwek et al. 2010). Alternatively, the dust could reside in the dense UVO knots and be heated by the radiative shocks that are propagating through the knots.

Overall, we are now witnessing the interaction of the SN blast wave with its surrounding medium, creating an environment that is rapidly evolving at all wavelengths. Since its explosion, SN 1987A has evolved from an SN dominated by the emission from the radioactive decay of ^{56}Co , ^{57}Co , and ^{44}Ti in the ejecta to an SNR whose emission is dominated by the interaction of the SN blast wave with its surrounding medium (Larsson et al. 2011). The latter consists of an ER flanked by two outer rings (Burrows et al. 1995), possibly part of an hourglass structure (Chevalier & Dwarkadas 1995; Sugerman et al. 2005).

The collision between the ejecta of SN 1987A and the ER predicted to occur sometime in the interval 1995–2007 (Borkowski et al. 1997; Gaensler et al. 1997) is still underway. At UVO wavelengths, “hot spots” have appeared inside the ER (Pun et al. 1997), and their brightness varies on timescales of a few months (Lawrence et al. 2000). New hot spots have continued to appear as the entire inner rim of the ER has become lit up by the interaction with the blast wave. HST images with equivalence to the *R* band (WFPC2/F675W, ACS/F625W, and WFC3/F675W; see Larsson et al. 2021) obtained between 1994 and 2009 revealed a necklace of such hot spots, nearly filling a lighted ring. Monitoring at X-ray wavelengths with the XMM-Newton, Chandra, and at radio frequencies, showed that while soft X-rays followed the optical and IR evolution, reaching maxima at 8000–10,000 days, hard X-rays and radio have shown a steady increase in the flux (e.g., Figure 4 in Alp et al. 2021).

Since ~ 5000 days post-explosion, bright multiwavelength emission has been produced by the shock interaction between the ER and ejecta (McCray & Fransson 2016). This is observed to currently be fading in IR, optical, and soft X-ray emission (Fransson et al. 2015; Larsson et al. 2019; Arendt et al. 2020; Alp et al. 2021; Maitra et al. 2022), suggesting that shocks are disrupting the dense ER and that the blast wave has passed through it (Fransson et al. 2015). The free expansion of the dense inner ejecta has simultaneously continued within the ER, revealing a highly asymmetric distribution in progressively greater detail.

The recent JWST data have provided us with unprecedented information on the mid-IR properties of this system. The Mid-Infrared Instrument (MIRI) onboard JWST provides imaging and spectroscopic observing modes from ~ 5 to 28 μm . The imaging mode is acquired with the so-called MIRIM instrument (Bouchet et al. 2015). In this paper, we will, for the first time, explore the iconic SN 1987A by investigating the heterogeneity of its temperature, morphology, and composition. In Section 2 we describe the observational program, and in Section 3 we present the results of the MIRIM data, including maps of the temperature variations. We discuss the findings of this paper in Section 4, including a description of efforts to locate the compact object left behind from the explosion (Section 4.1), as well as examinations of emission outside the ER and that of the outer rings (Section 4.2). Section 5 presents our summary and conclusions. Finally, details of the reduction method are described in Appendix.

2. Observations

SN 1987A was observed with MIRI on 2022 July 16, corresponding to day 12,927 after outburst, as part of guaranteed time program #1232 (PI: G. Wright). Due to the brightness of the target, the subarray BRIGHTSKY, with 512×512 pixels, was chosen instead of the 1024×1024 pixel full field of view of MIRI, which has a detector plate scale of $0''.11 \text{ pixel}^{-1}$.

As the ER has a diameter of slightly over 2 arcsec (~ 20 pixels), the size of our region of interest is well within the dimensions of this subarray. Note as well that utilizing BRIGHTSKY lowers the sampling time from 2.775 seconds to 0.865 seconds, allowing for longer ramps for our observations. We obtained images taken with four different filters: F560W, F1000W, F1800W, and F2550W, which were chosen to sample MIRI’s full 5–28 μm wavelength coverage.

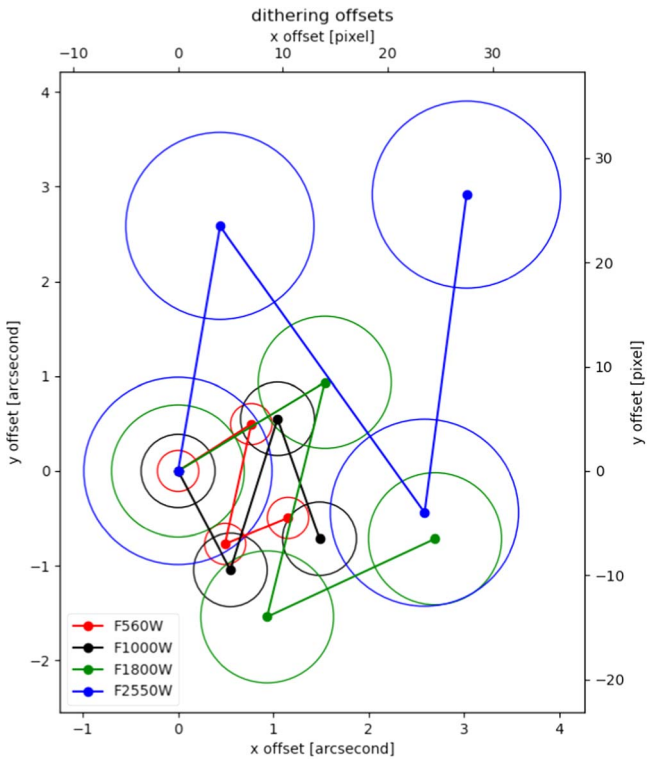


Figure 1. Illustration of the dithered positions for each of the four filters, with the Airy disk corresponding to each wavelength shown. The radius of the disks is $1.22 \lambda/D$, with $D = 6.50$ m (reminder: this is the radius of the first black ring).

The length of each integration (number of frames taken) was 16 for F560W and 15 for the other filters where fluxes are higher; these lengths were chosen so that the bright pixels would not saturate. The number of integrations was 18 for F560W, 17 for F1000W and F1800W, and 20 for F2550W (see Ressler et al. 2015 for an explanation of the MIRI readout sensor chip assembly). For each filter, we used the standard MIRI dither pattern with four positions as shown in Figure 1, which also displays the Airy disk for each filter. As this was one of the earliest uses of MIRI’s subarray observation mode BRIGHTSKY, we describe in the appendix the steps that were taken to reduce the data.

3. Results

3.1. Images

Our data treatment produces the images shown in Figure 2, which shows the BRIGHTSKY mode’s 512×512 pixel field of view in each of the F560W, F1000W, and F1800W filters, together with a false-color image produced from those three filters. The images show extended nebulosity, mostly toward the edges of the field, around a cavity with an angular diameter of $\sim 30''$ that appears to surround SN 1987A.

Figure 3 shows the central 65×65 pixels in each of the F560W, F1000W, F1800W, and F2550W filters. For each filter, we have superimposed the MIRI-MRS image contours of the strong [Ar II] $6.985 \mu\text{m}$ line (Fransson et al. 2024), which were derived from the data presented in Jones et al. (2023). Table 1 lists the in-band photometric fluxes measured for each of the four filters for SN 1987A’s ER and ejecta. These were measured using the same on-source and background apertures as defined by Jones et al. (2023) for their “total” MRS spectrum

of SN 1987A. An updated version of the “total” MRS spectrum is shown in Figure 4. The raw data have been reprocessed using updated calibration reference files which primarily affect the shape of the spectrum at longer wavelengths. The reprocessed data and spectrum will be presented in a future work. The uncertainty in the MIRIM absolute flux calibration is estimated to be around 3%–5% (K. Gordon et al 2024, in preparation). The equivalent filter fluxes obtained by convolving the MRS spectrophotometry with the photon conversion efficiency profiles for each filter plotted in Figure 4 are also listed in the table. In the case of the F2550W filter, the MRS spectrophotometric calibration cuts off at $27 \mu\text{m}$, below the upper limit of the F2550W filter at $\sim 30 \mu\text{m}$. We therefore extrapolated the continuum above $27 \mu\text{m}$ using a second-order polynomial fit to the continuum in the $23\text{--}27 \mu\text{m}$ range to account for “missing” flux in the MRS spectrum that would be detected by MIRIM. The uncertainty in the MRS absolute spectrophotometric flux calibration is estimated by Argyriou et al. (2023) to vary from 4% at its shorter wavelengths (Bands 1 and 2) to 5% (Band 3) and 6% (Band 4) at its longer wavelengths. The MIRIM and equivalent MRS photometric fluxes are plotted as the blue and red solid symbols in that figure. Inspection of Table 1 shows excellent agreement between the Imager and equivalent MRS filter fluxes in the cases of the F560W and F1000W filters, and good agreement for the F1800W and F2550W filters. The F2550W band includes the strong [Fe II] $25.99 \mu\text{m} + [\text{O IV}] 25.89 \mu\text{m}$ feature (see Figure 4), but, as listed in the last row of Table 1, we find that these and other emission lines contribute only 2.9% of the total in-band flux in the F2550W filter. We estimated the contributions of the emission lines in a given filter by comparing the calculated in-band flux of the spectrum with and without these lines. For the latter, we masked the emission lines and interpolated the continuum across the resulting gaps using a second-order polynomial. The F560W filter has a much weaker continuum, but even for that filter emission lines are found to contribute only 1.9% of the total in-band flux. For the F1000W and F1800W filters, emission lines make a negligible contribution (Table 1). The contributions of synchrotron and free–free emission are also small except perhaps at wavelengths shorter than $8 \mu\text{m}$ (Jones et al. 2023). It would seem that the most likely explanation for the small discrepancy at the two longest wavelengths between the Imager filter fluxes and the equivalent MRS filter fluxes is a difference in the background estimation, given that background flux levels rise steeply to longer wavelengths.

Larsson et al. (2011), Helder et al. (2013), and Frank et al. (2016) reported on the brighter optical and X-ray emission in the western regions of the ring. As already seen at optical wavelengths (Fransson et al. 2015), a comparison of the day 6526 11.7 and $18.3 \mu\text{m}$ images of Bouchet et al. (2006) with the new JWST images taken at day 12927 shows that the emission from the NE region of the ring has fallen dramatically and the strongest emission from the ring now arises from the SW region. This seems to indicate that most of the dust that was lying in the NE region has been either destroyed or has recently cooled after the passage of the shock. The change in brightness alone does not permit us to distinguish between the two scenarios.

In Figure 5 we have superimposed on our image obtained through the F2550W filter the contours of the [Fe II] $\lambda 25.99 \mu\text{m}$ line from the MRS data. The MRS data clearly showed that this

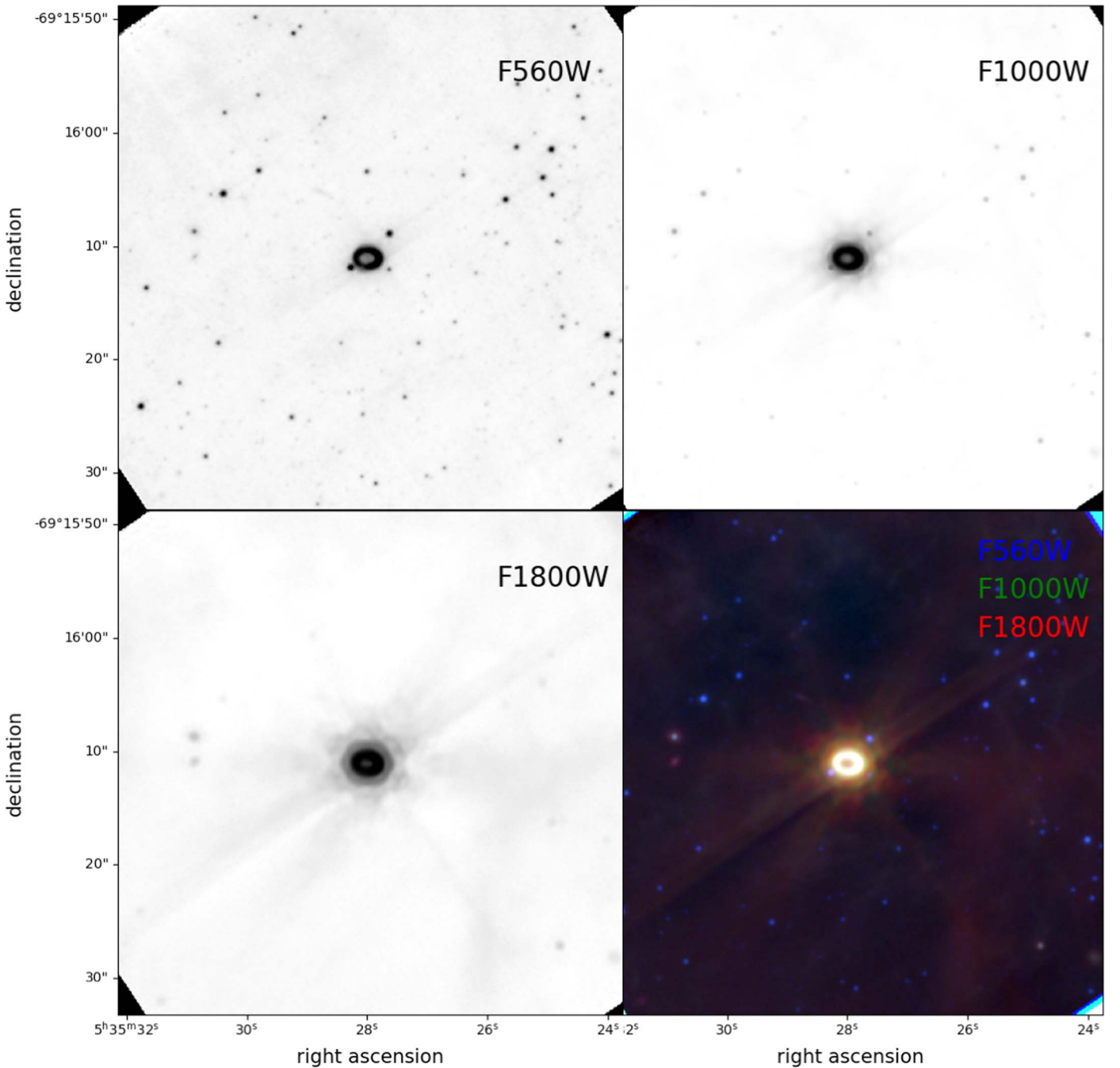


Figure 2. MIRI images of the full 512×512 BRIGHTSKY subarray. Images with the F560W, F1000W, and F1800W filters are shown in the top row and in the bottom left panel. The F2550W image is not shown. The bottom right panel shows a false-color image produced from the three filters with RGB = F1800W, F1000W, and F560W.

prominent line is coming mostly from the inner ejecta and the ejecta close to the reverse shock (Jones et al. 2023), while the dust which dominates the F2550W filter is from the ring. The Imager data, which have a spatial resolution ~ 2 times better than the MRS data, confirm this conclusion, with the dust-dominated F2550W image showing a drop in emission inside the ER, whereas the $[\text{Fe II}]\lambda 25.99$ -dominated contours peak inside the ER.

3.2. Temperature and Mass Maps

Several dust composition models have been proposed for SN 1987A. After the far-IR Herschel observations revealed a large reservoir of cold dust, Matsuura et al. (2015) proposed a mix of

amorphous carbon and silicates, which yields $T_{\text{Dust}} \sim 23\text{--}27$ K and $M_{\text{Dust}} \sim 0.3\text{--}0.8 M_{\odot}$, depending on whether the composition arises solely from amorphous carbon or a mix with silicates.

Cigan et al. (2019) comment on the Atacama Large Millimeter/submillimeter Array (ALMA) images and conclude that the submillimeter emission coming from the inner region is due to thermal emission from the ejecta which was first pointed out by Indebetouw et al. (2014), and then Cendes et al. (2018) included synchrotron emission.

Computing a temperature map based on a simple blackbody emission should apply for optically thick emission from the

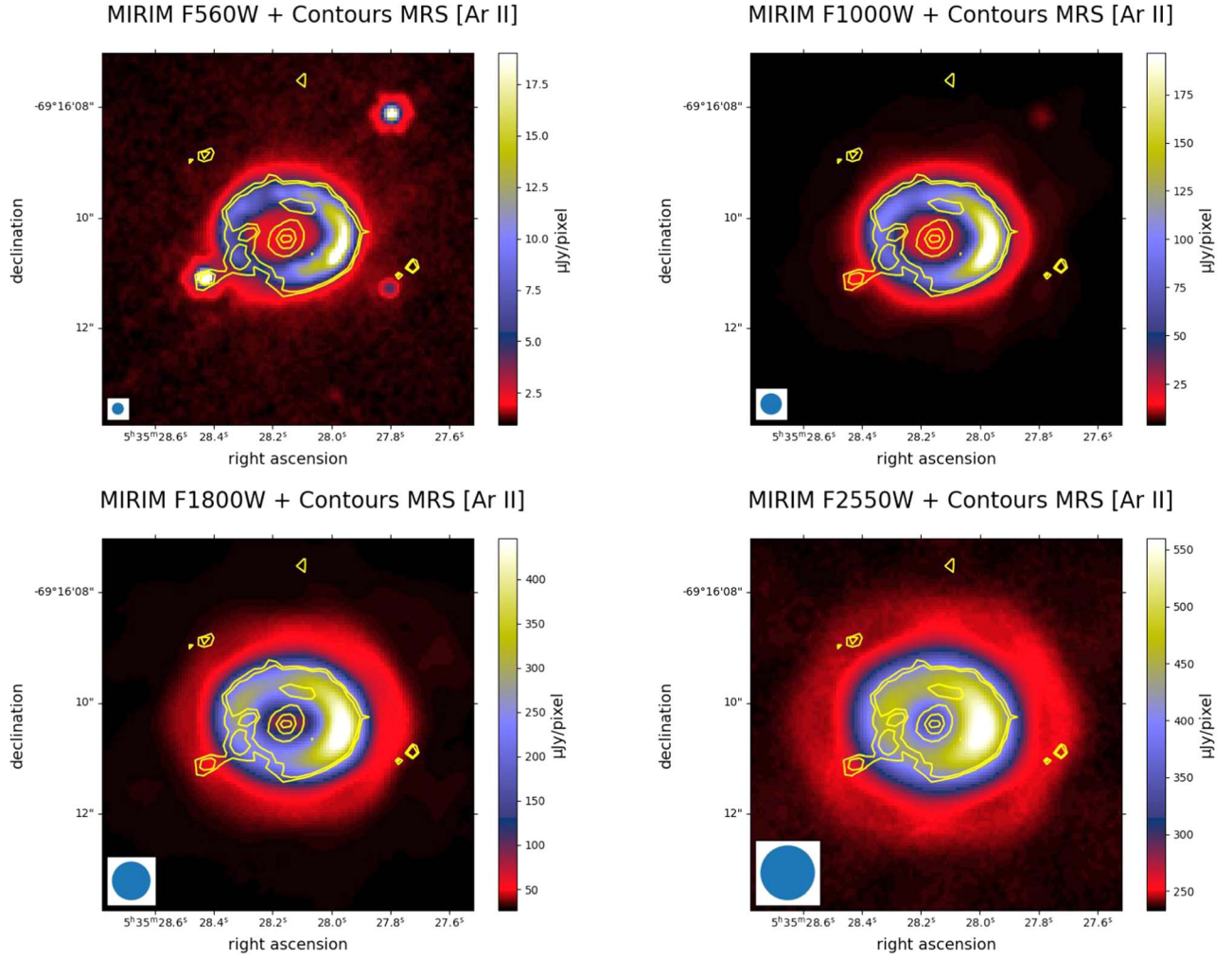


Figure 3. Final processed images at 5.6, 10, 18, and 25.5 μm , on which we superimpose the MRS [Ar II] 6.985 μm contours in white. Contours levels: [90, 100, 200, 600, 1000 MJy sr^{-1}]. The corresponding clean beams (Gaussian fit of the actual PSF) for each wavelength are shown in the lower left corners.

Table 1

Filter Fluxes for SN 1987A from the MIRIM and Equivalent Fluxes from the MRS Spectrophotometry (See Text)

Flux (mJy)	F560W	F1000W	F1800W	F2550W
Imager	1.8 ± 0.1	29.3 ± 0.1	105.9 ± 0.3	110.2 ± 1.4
MRS	2.4 ± 0.6	31.1 ± 0.3	106.2 ± 0.5	118.3 ± 5.0
Line Contribution	1.9%	$\lesssim 0.1\%$	$\lesssim 0.1\%$	2.9%

ejecta only. Moreover, fitting a blackbody model to the mid-IR observations is not justified as the mid-IR fluxes are dominated by optically thin emission from silicate dust grains in the ER (Arendt et al. 2016; Jones et al. 2023).

For an optically thin point source, the flux density, $F_\nu(\lambda)$ at wavelength λ is given by Hildebrand (1983) and Bouchet et al. (2006)

$$F_\nu(\lambda) = 4M_d \frac{\kappa(\lambda) \pi B_\nu(\lambda, T_d)}{4\pi D^2},$$

where M_d is the dust mass, $\kappa(\lambda)$ is the dust mass absorption coefficient at wavelength λ , $B_\nu(\lambda, T)$ is the Planck function, and D is the distance to the supernova, taken to be $D = 51.4$ kpc (Panagia et al. 1991).

We first fitted the integrated MIRI flux densities with a population of dust particles consisting of a single population of silicate and amorphous carbon grains to account for the shorter wavelengths emission as explained in Bouchet et al. (2006) and Arendt et al. (2016). We used carbon and silicate dust mass absorption coefficients from Draine & Lee (1984); see Figure 6), with results shown in Figures 7 and 8 (the four filters have been used to generate these maps). The temperature computed from this model varies from 120 to 165 K and the mass varies from 0.2 to $1.5 \cdot 10^{-8} M_\odot \text{ pixel}^{-1}$. The total mass, that is the sum of the pixels enclosed by the contours (equatorial ring) is then $1.3 \pm 0.5 \cdot 10^{-5} M_\odot$, similar to the mass reported by Jones et al. (2023) for the same day ($1.5 \pm 0.3 \cdot 10^{-5} M_\odot$). It is striking to note that although the temperature is similar, the total mass of the dust is ~ 10 times greater than those reported by Bouchet et al. (2006). It should be emphasized that the essential difference between these two dates is the amount of material that interacts with the ER. Bouchet et al. (2006) report masses of $0.1 - 0.2 \pm 0.03 \cdot 10^{-5} M_\odot$ at days 6070 and 6190 and $0.3 \pm 0.1 \cdot 10^{-5} M_\odot$ at day 6525, which approximately marks the onset of the interaction of the ejecta with the equatorial ring and the dust mass in the ER. Jones et al. (2023) report that this mass was already $0.85 \pm 0.15 \cdot 10^{-5} M_\odot$ at day 6805, then increased linearly until day

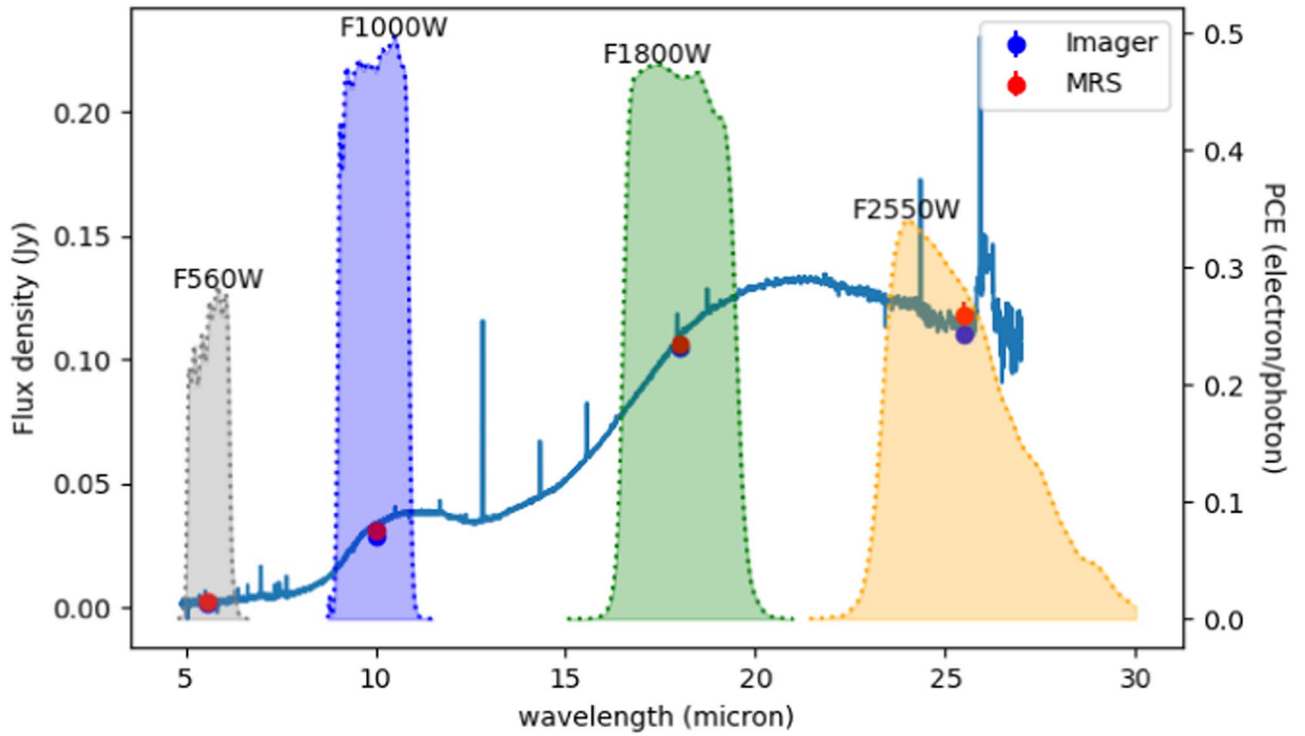


Figure 4. The “total” MRS spectrum of SN 1987A is shown, together with the photon conversion efficiency (PCE) profiles for the four filters used in MIRI imaging observations. The actual PCE of the F2550W filter extends to $\sim 30 \mu\text{m}$, beyond the plotted MRS calibration limit. The blue filled circles correspond to the measured MIRIM in-band photometric fluxes, while the red filled circles correspond to equivalent in-band fluxes obtained by convolving the MRS spectrophotometry with the filter PCE profiles.

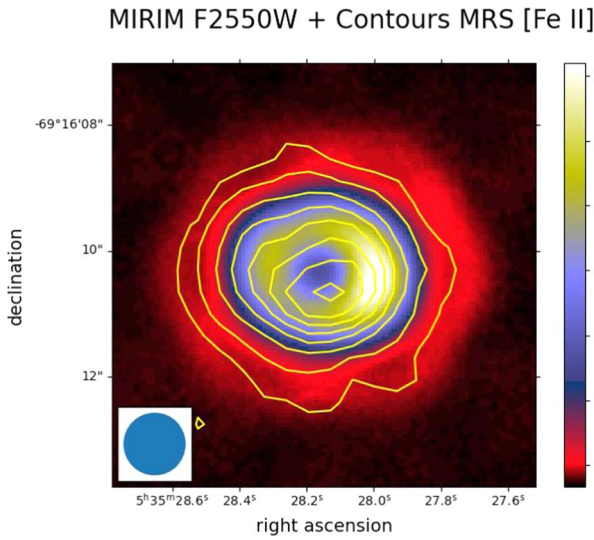


Figure 5. MIRIM image in the F2550W filter, with the white contours showing the distribution of the [Fe II] $25.99 \mu\text{m}$ + [O IV] $25.89 \mu\text{m}$ emission from the MRS data. Contours levels: [900, 1000, 1200, 1400, 1600, 1800, 2000, 2200 MJy sr^{-1}].

7955 (during that period this linear increase is fitted by: $M_{\odot} = 4.77 \cdot 10^{-4} \times t_{\text{Day}} - 2.37$), to remain constant up to day 12,927 (Table 2 and Figure 9 summarize the dust mass evolution). That means that the interaction of the ejecta with the ER was accompanied by an increase in dust mass. As a result, we have two possible explanations: (i) either this interaction makes a new condensation of grains, (ii) or a fraction of the very cold dust initially in the ejecta has warmed up in the ring environment and therefore the mass of warm dust increased

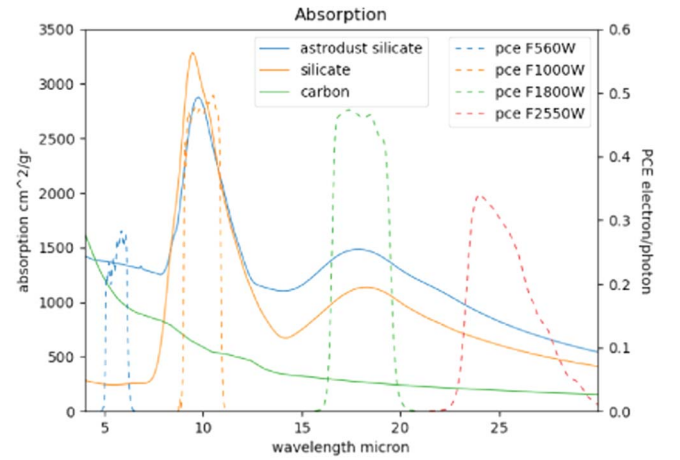


Figure 6. Dust mass absorption coefficients for some of the grain species (references in the text) and the photon-to-electron conversion efficiency (PCE) for each filter.

while that of very cold dust detected by Herschel and ALMA would have decreased (future ALMA observations should confirm this hypothesis).

We also generated dust temperature and mass maps using the so-called astro dust model, as described by Hensley & Draine (2023) and applied to SN 1987A by Jones et al. (2023). Results are shown in Figure 10 and Figure 8 (as for Figure 7 the four filters have been used to generate these maps). The temperature varies from 125 to 175 K, quite consistent although slightly warmer than the temperatures computed from the silicates model, and the mass varies from 0.5 to $3.5 \cdot 10^{-8} M_{\odot} \text{ pixel}^{-1}$. The total mass using the astro dust composition is then

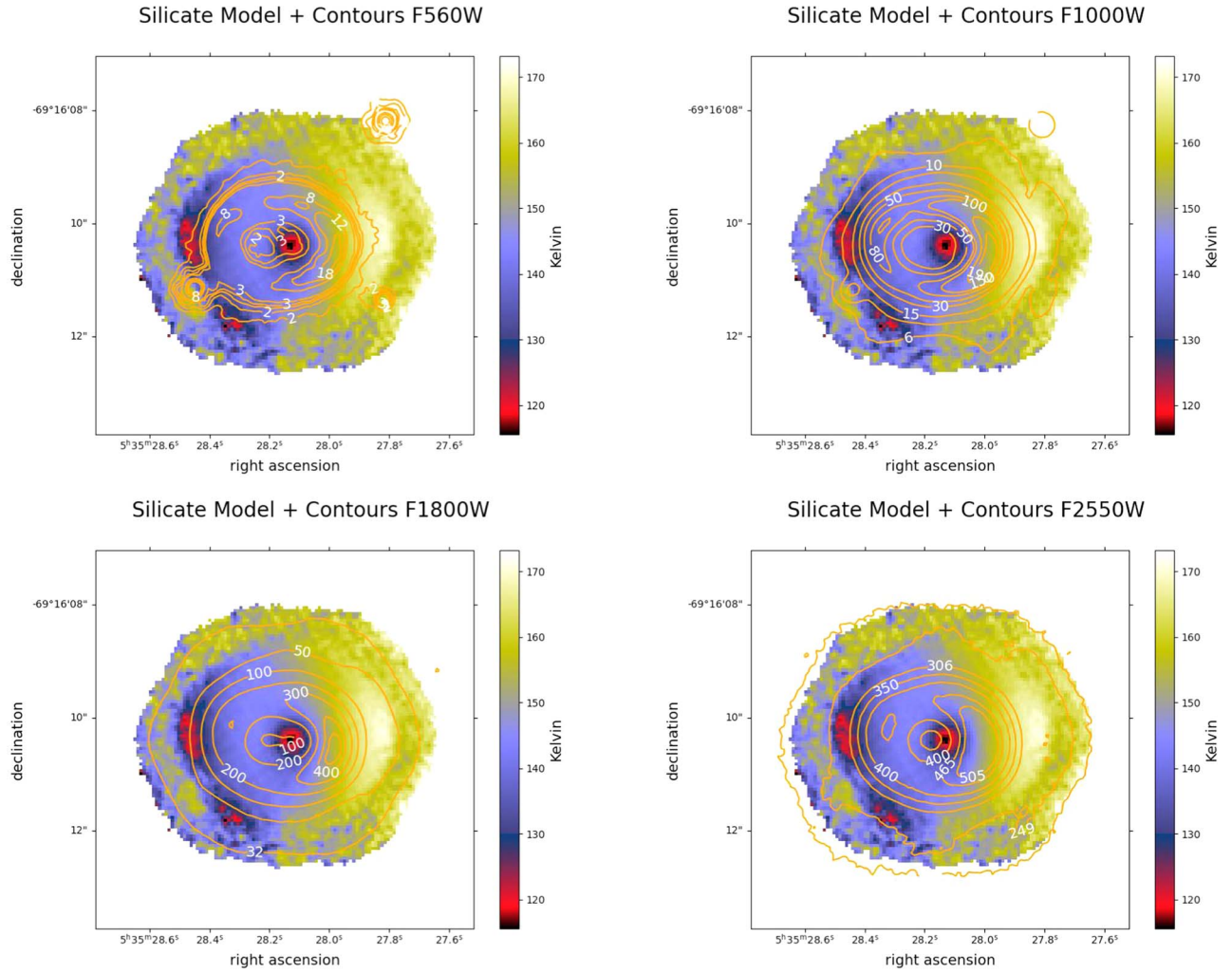


Figure 7. Temperature map computed with the silicates and amorphous carbon model as discussed in the text, with contours from the four images. Contour levels: F560W: [1.5, 2.2, 2.4, 2.7, 3.2, 8, 12, 18 $\mu\text{Jy pixel}^{-1}$]; F1000W: [6, 10, 15, 30, 50, 80, 100, 150, 190 $\mu\text{Jy pixel}^{-1}$]; F1800W: [35, 50, 100, 200, 300, 400, 450 $\mu\text{Jy pixel}^{-1}$]; F2550W: [240, 248.6, 306, 350, 400, 465, 505 $\mu\text{Jy pixel}^{-1}$].

Table 2
Evolution with Time of the Dust Mass in the ER

Day	Mass($10^{-5} M_{\odot}$)	Reference
6070	0.20 ± 0.10	Bouchet et al. (2006)
6190	0.12 ± 0.05	Bouchet et al. (2006)
6526	0.30 ± 0.10	Bouchet et al. (2006)
6805	0.85 ± 0.12	Jones et al. (2023)
7138	1.10 ± 0.10	Jones et al. (2023)
7296	1.10 ± 0.10	Jones et al. (2023)
7555	1.20 ± 0.10	Jones et al. (2023)
7799	1.40 ± 0.20	Jones et al. (2023)
7955	1.40 ± 0.20	Jones et al. (2023)
12997	1.50 ± 0.30	Jones et al. (2023)
12997	1.30 ± 0.30	Present work

$2.8 \cdot 10^{-5} M_{\odot}$, significantly higher than the mass reported by Jones et al. (2023; $1.7 \pm 0.2 \cdot 10^{-5} M_{\odot}$).

Note that the contours shown in Figures 7 and 10 delineate the ER, within which the models make sense. The composition of the dust beyond the ER is not known, and it is doubtful that the models can apply. Both models show that the warmest temperatures are located on the outer edge west of the ER.

The comparison of the mass absorption coefficient for each of the grain species is shown in Figure 6.

In order to estimate temperatures (electron, ER, and ejecta), Jones et al. (2023) use various line ratios. According to these authors, the strongest emission line in the F1800W MIRIM filter is the [Fe II] 18.93 μm line from the ER, while the F2550W filter includes the prominent [Fe II] 26 μm emission line from the ejecta. In the same vein as these authors, we produce an F2550W-to-F1800W ratio image (after blurring the F1800W image to the lower resolution of the F2550W image; see Figure 11), and we derive a temperature map using these two filters only with the astro dust model (Hensley & Draine 2023). The result is shown in Figure 12. Although the dust temperature range of 105–140 K is consistent with the previous calculation made with the four filters (Figure 10), the west side of the ER appears slightly cooler in this computation. Note that part of this result should be taken with caution, for it is doubtful that we can use the astro dust model to derive temperatures in the ejecta. Also, according to Jones et al. (2023), we need two-grain components to reproduce the emission, so it is clear that a single temperature fit across the entire SED might be too influenced by the changing mass of the small grain component.

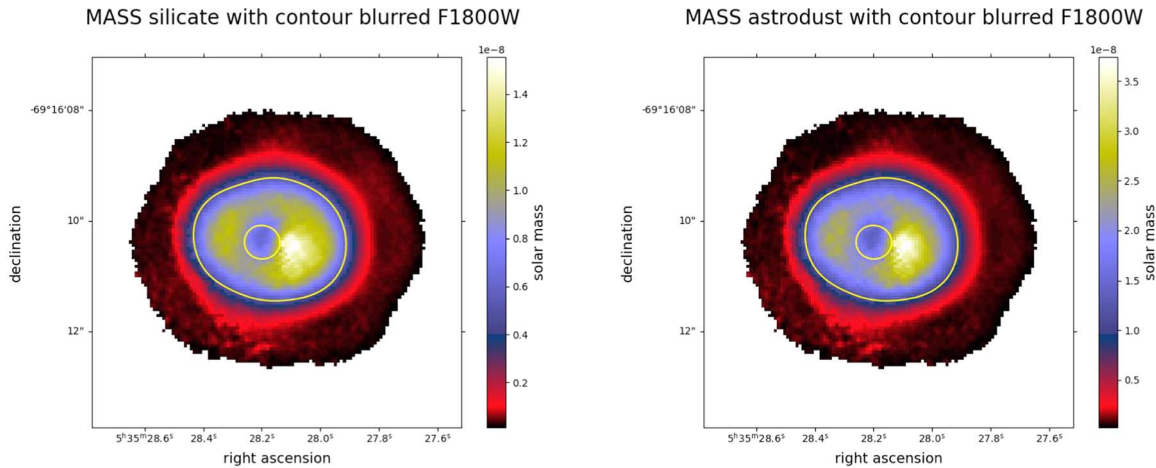


Figure 8. Mass maps computed with the two dust grain compositions: silicates (left) and astroduct (right). The contour level is $150 \mu\text{Jy pixel}^{-1}$, which delimits the equatorial ring (the total mass is the sum of the pixels enclosed by the contour).

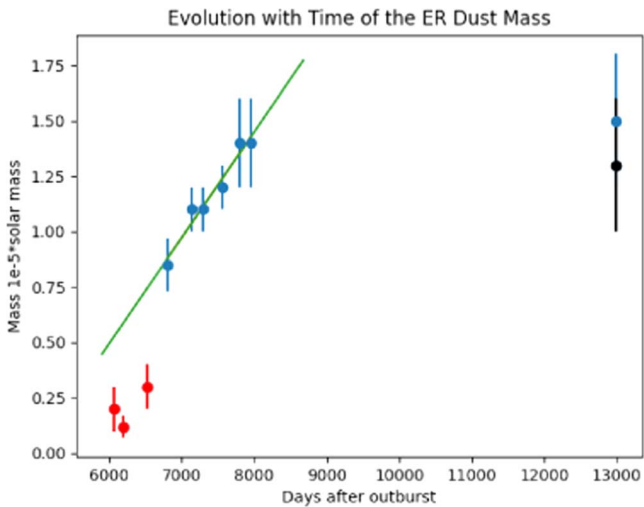


Figure 9. Evolution with time of the ER dust mass (red dots are from Bouchet et al. (2006); blue dots are from Jones et al. (2023); the black dot is from the present work. The linear increase during the period [6805, 7955] day is fitted by: $M_{\odot} = 4.77 \cdot 10^{-4} \times t_{\text{Day}} - 2.37$).

4. Discussion

4.1. Searching for the Compact Object

The progenitor of SN 1987A, Sanduleak -69 202, was a blue supergiant (Gilmozzi et al. 1987; Kirshner et al. 1987; West et al. 1987; White & Malin 1987), thought to have had a zero-age main-sequence mass of $\sim 19 M_{\odot}$ (Woosley et al. 1987; Hashimoto et al. 1989), with a mass of $\sim 14 M_{\odot}$ at the time of the explosion (Woosley 1988; Smartt et al. 2009; Sukhbold et al. 2016). From its mass, the expectation is that a compact object should have formed at the time of the explosion. Despite prompt neutrino emission observed at the burst (Alekseev et al. 1987; Bionta et al. 1987; Hirata et al. 1987) indicating the presence of a neutron star (NS; Burrows 1988; Sukhbold et al. 2016), the search for a compact object associated with SN 1987A has been the grail of a long and continuous search. All the observational searches have thus far proven unfruitful (e.g., Manchester 2007; Alp et al. 2018; Zhang et al. 2018).

The detection of radio polarization by Zanardo et al. (2018) hints at the presence of magnetized shocks, potentially due to a

compact object. Alp et al. (2018) proposed that a thermally emitting NS could be dust-obscured and that this may be detectable as a point source in far-IR or submillimeter images of the remnant. Our MIRI images have not shown any evidence for such a point-like object.

Cigan et al. (2019) detected with ALMA a dust peak “blob” that they attributed to either a pulsar wind nebula (PWN) or to a clump heated by ^{44}Ti decay. They argue that the most probable explanation is that the innermost region of dust and gas is heated by radiation from the NS, with early development of a PWN, and propose that the identified central “blob” is due to warm ejecta heated by the NS. Notwithstanding, they note that the ALMA data cannot disentangle whether the heating originates from grains heated directly by thermal X-rays from the NS, as in Alp et al. (2018), or by synchrotron radiation generated by the NS.

Figure 13 shows the ALMA images at 315 and 679 GHz with contours from the MIRI images and the position of the warm “blob” found by Cigan et al. (2019). We, however, do not find any obvious correspondence between the position of this in the ALMA images and any enhancement in the MIRI images.

In Fransson et al. (2024) a strong point source at the center of SN 1987A is found at $6.9861 \mu\text{m}$, which is identified with the [Ar II] $6.9853 \mu\text{m}$ line, blueshifted by $\sim 253 \text{ km s}^{-1}$. In addition, weaker lines from [Ar VI] $4.529 \mu\text{m}$, [Ar III] $8.991 \mu\text{m}$, [S IV] $10.51 \mu\text{m}$, and [S III] $18.71 \mu\text{m}$ are identified. The position, the low radial velocity, and the fact that this source is only seen in lines of highly ionized S and Ar show that the emission is originating in the explosive oxygen burning zone, dominated by Si, S, Ar, and Ca and that the ionizing source is likely to be the central NS in SN 1987A. The exact nature of this is not yet clear. Candidates are the thermal emission from the cooling NS, the nonthermal emission from a PWN, the shock from the expending PWN bubble, or a combination of these. In any case, the presence of a compact object is strongly indicated. With this background, it is therefore natural to look for a corresponding point source in the MIRI images.

Unfortunately, neither the F560W nor the F1000W filters cover the [Ar II] $6.985 \mu\text{m}$ line, which is by far the strongest of the above lines and in addition is less contaminated by the strong dust continuum background at the longer wavelengths. The other lines have fluxes $\gtrsim 4\%$ of this line and are dominated

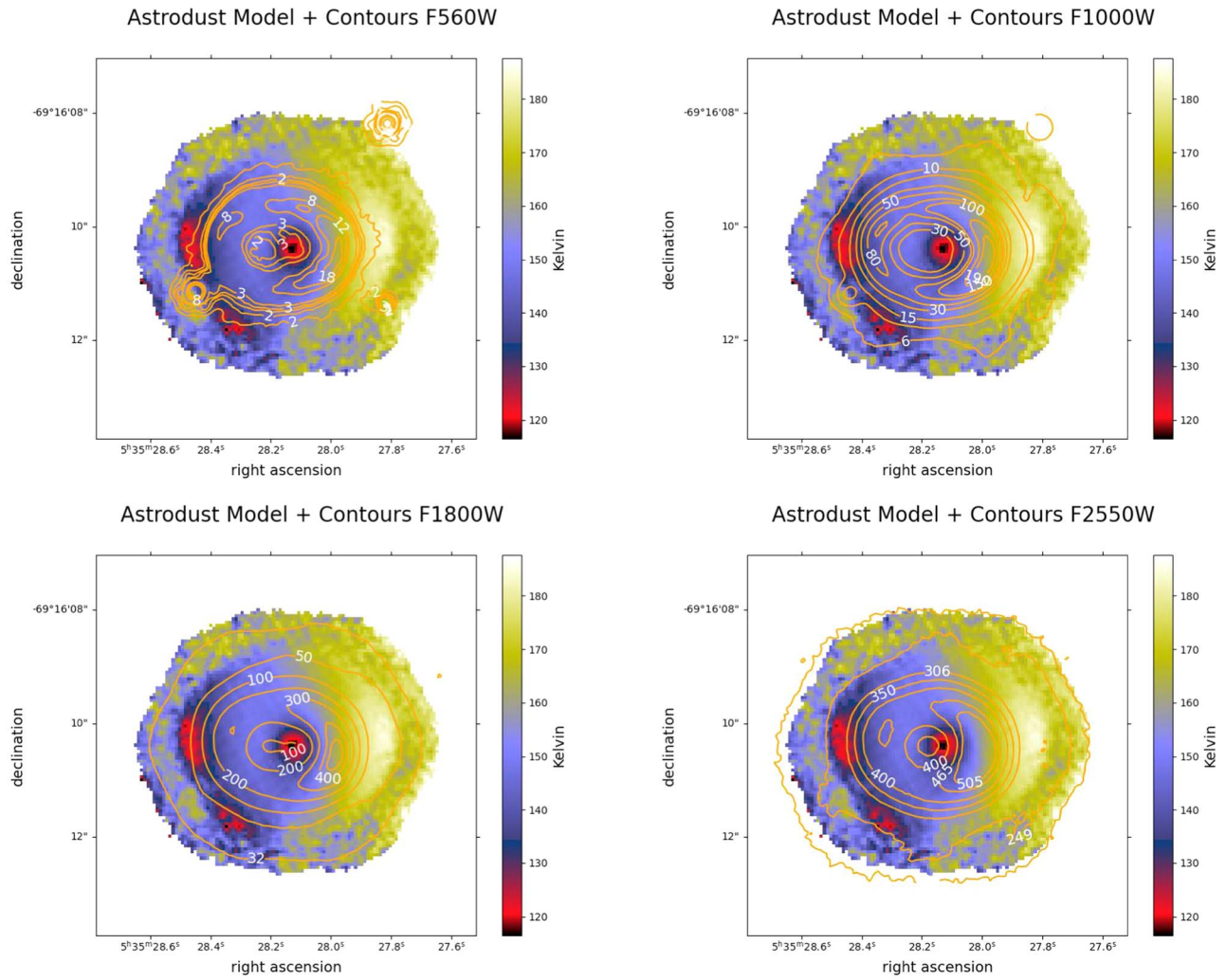


Figure 10. Temperature map computed with the astrodust model with the data from the four filters as discussed in the text, with contours from the four images as in Figure 6. Contour levels are indicated in the figure.

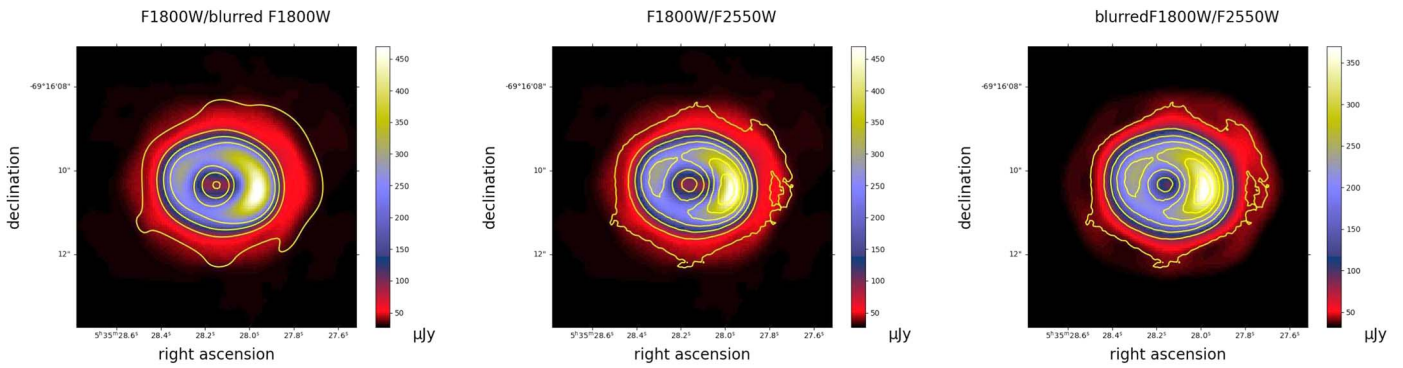


Figure 11. Left: MIRI image obtained with the filter F1800W with contours from the same image blurred at the resolution of the F2550W image; middle: image obtained with the filter F1800W with contours from the F2550W image; right: image obtained with the filter F1800W blurred at the resolution of the F2550W filter and contours from the F2550W image.

by the dust background in the filters. It is therefore not surprising that no point source corresponding to these lines is seen in the observed filters. Imaging in the F770W filter, which contains the [Ar II] 6.985 μm line, would be the most promising MIRI filter to reveal more details about the central emission source.

The F560W image shows a detection of emission from the ejecta. To highlight the structure within the ejecta more clearly we deconvolved the image with the Richardson–Lucy algorithm, using the WebbPSF model. The result is shown in Figure 14, showing an emission region just north of the center and a curved region of lower surface brightness just below it. This

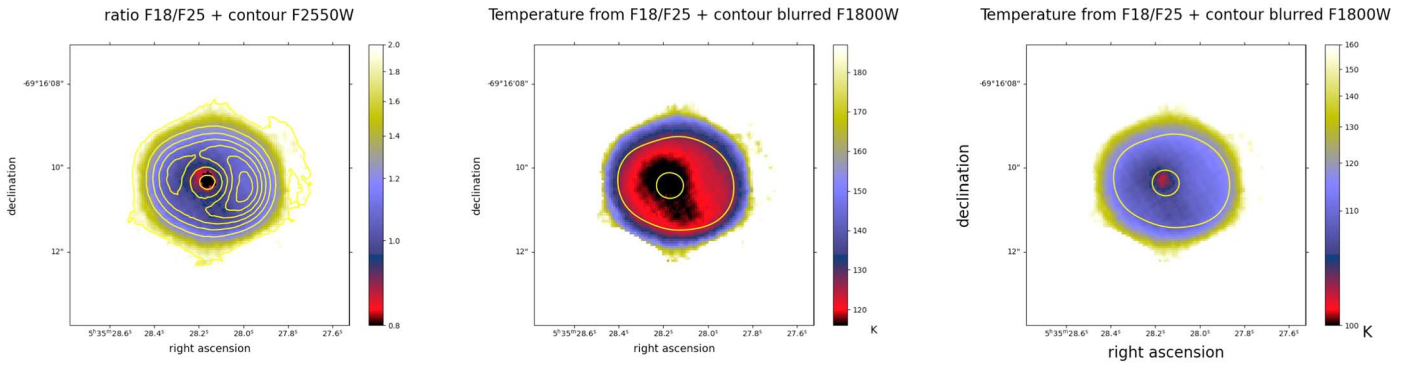


Figure 12. Left: ratio of the blurred F1800W over the F2550W images, with contours from the F2550W image [250, 300, 350, 400, 450, 500, 550 $\mu\text{Jy pixel}^{-1}$]; middle: temperature map computed with the astrodust model applied to the F1800W over the F2550W filters ratio, with contours from the blurred F1800W image. To compare with Figure 10. Contour levels are 150 $\mu\text{Jy pixel}^{-1}$, defining two ellipses that enclose the ER; right: same as the middle figure with a logarithmic color scale in order to pinpoint the central region.

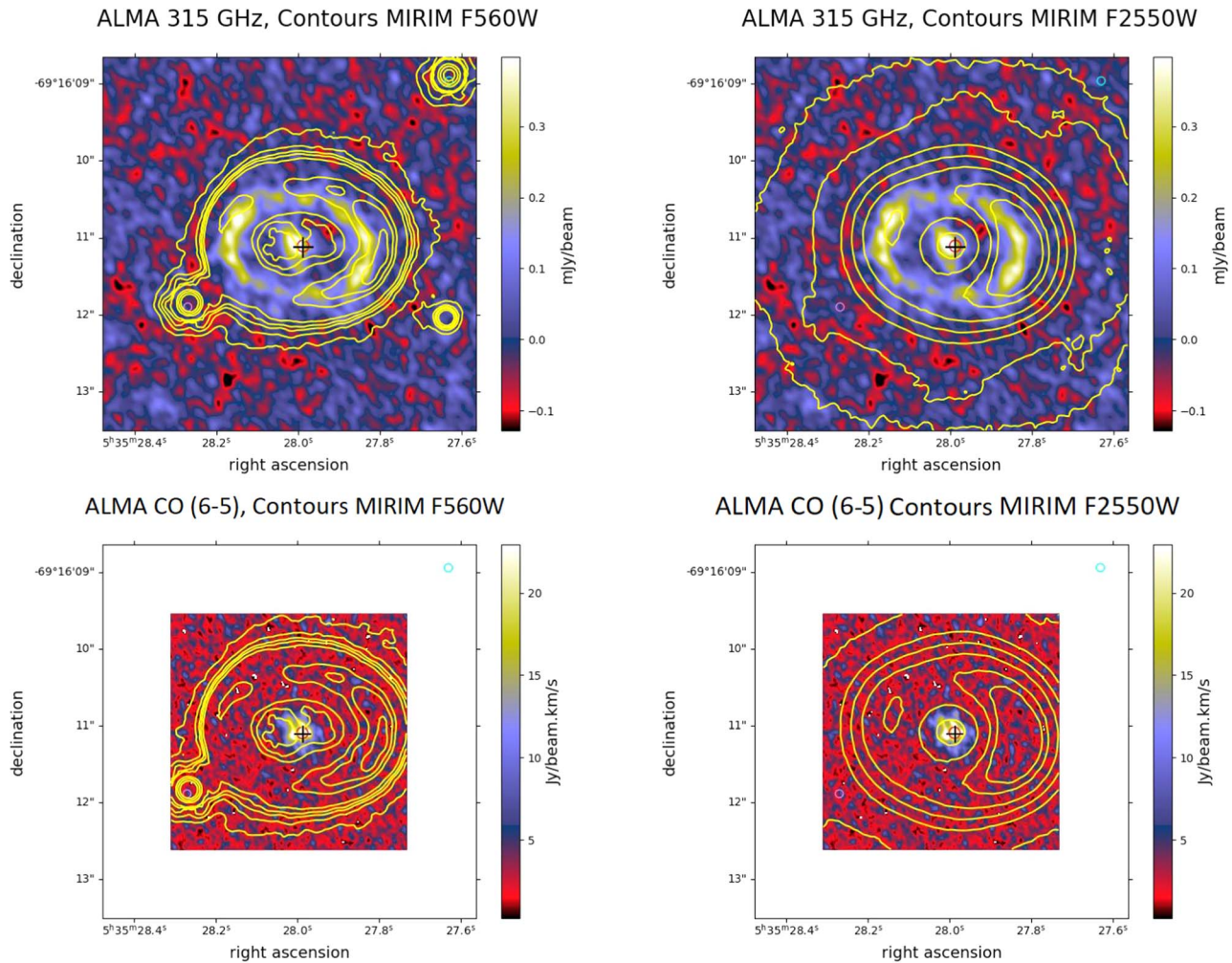


Figure 13. ALMA images at 315 GHz (952 μm) and in the CO (6-5) band at 641.47 GHz (467 μm); contours from the MIRI images as indicated, with the position of the submillimeter dust “Blob,” proposed by Cigan et al. (2019) to be heated by a neutron star candidate denoted with a cross.

morphology is very similar to that observed in the NIRCcam F323N and F356W filters (Arendt et al. 2023), which are dominated by continuum emission in the ejecta region (see spectra in Larsson et al. 2023). Figure 14 also includes contours from the ALMA 315 GHz image which probes cold dust, the dust “blob” at 679 GHz that Cigan et al. (2019) attribute to heating by the compact object, and the MRS [Ar II] 6.9853 μm

line associated with the compact object. The [Ar II] emission is centered south of the emission region in the F560W image.

4.2. Emission Outside the ER

In the MIRI images, the ER is not as well defined in the mid-IR now as it was in past years (Bouchet et al. 2006). Instead,

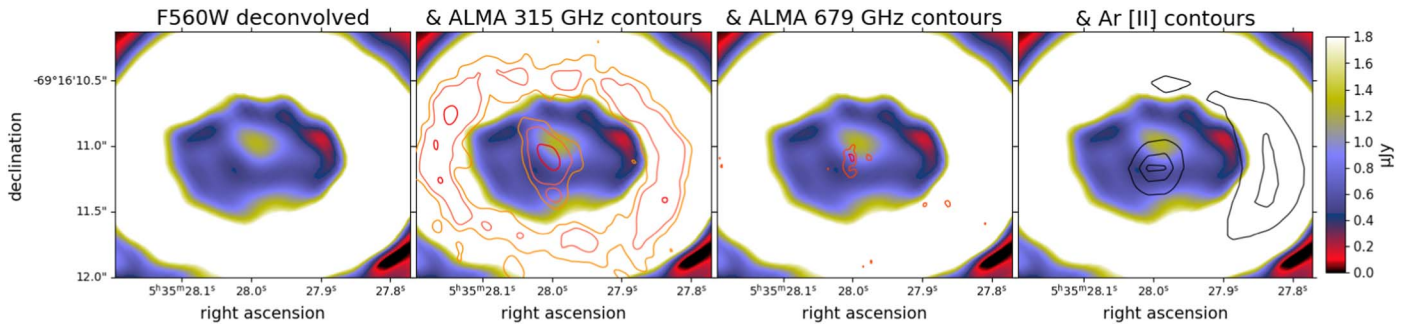


Figure 14. MIRI F560W image, deconvolved with the Richardson–Lucy algorithm. The color scale is set to highlight the faint ejecta. The second, third, and fourth panels from the left show this image together with contours from the ALMA 315 GHz image, the ALMA 679 GHz image, and the MRS [Ar II] 6.9853 μm line, respectively. Note that the dust “blob” that Cigan et al. (2019) attribute to heating by the compact object can be seen in the third panel.

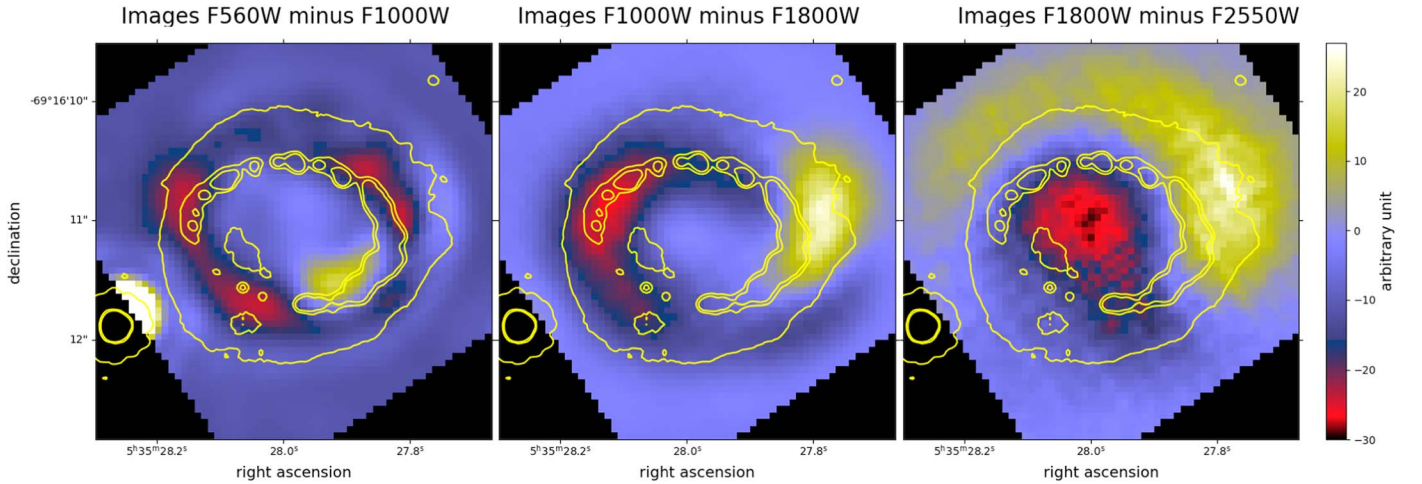


Figure 15. Recursive subtraction between adjacent filters to allow comparison of the flux evolution with wavelengths. Contours from the HST/WFC3 image from 2022 (Rosu et al. 2024) are drawn to illustrate the position of the ER. The negative fluxes are due to the subtraction between wavelengths. Contours levels: [0.06, 0.6, 1 electrons s^{-1}]. The HST image has been offset by [22, 20] pixels.

extended emission outside but adjacent to the ER is seen, whose size (width of ellipse) increases with the wavelength. The images at shorter wavelengths have been blurred to the spatial resolution of the following longer wavelength images, in order to show, via a recursive subtraction between adjacent filters, a comparison of the flux evolution with wavelength. The results are shown in Figure 15, which illustrates the increasing flux of the SW region with longer wavelengths, and also extension beyond the ER. These images are a good indication of the E–W temperature variation in the ER itself. Even though the inner ejecta are not directly seen in the individual images, this seems to indicate that they have a redder spectrum (possibly from [Fe II] emission) than the ER.

To deconvolve, we instead used a modified version of the CLEAN method (Högbom 1974), which looks for positive sources in the central region of the maps.

We also extracted templates from the images without the low-level extensions, then convolved those templates with the PSF and obtained the same kind of extensions.

It can be seen that at the longest wavelength (25.5 μm), the mid-IR emission apparently extends outside the known ER. Note that an extension beyond the knotty ER has been seen in the HST data for some years now (Fransson et al. 2015). The apparent extension in our MIRI images is however mostly the product of a PSF effect. Unfortunately, there is no PSF

available of sufficient quality at these wavelengths to make a reliable correction.

Results from our deconvolution of the MIRI images are presented in Figure 16, which shows clearly that the extension of the mid-IR emission seen in Figure 3 may not be real. In Figure 3 we see a red “skirt” growing with wavelength. For the F2550W filter, we find some structure in the red skirt. However, after our deconvolution using Högbom’s CLEAN algorithm, the structure vanishes (Figure 16). Note that the CLEAN algorithm does not enhance the resolution but replaces the dirty beam (with structure) with a “cleaned” beam fitted by a 2D Gaussian. We clearly see that the deconvolved F2550W image and the F560W image both contain a ring with a thickness of a few pixels.

When high-quality PSFs and efficient removal of odd/even row effects become available, it will be possible to redo this study with higher confidence, but for now, we consider that no evidence of extensions has been shown in these broadband images. We note, however, that evidence for extensions has been seen in MRS spectral channels that isolate fine-structure line emission (Jones et al. 2023).

Finally, no hint of the two outer rings can be seen in any of our four MIRI broadband images, although forbidden-line emission from the outer rings is seen at several wavelengths in the much higher resolving power MRS spectral images of SN 1987A (Jones et al. 2023) where we could only see the outer

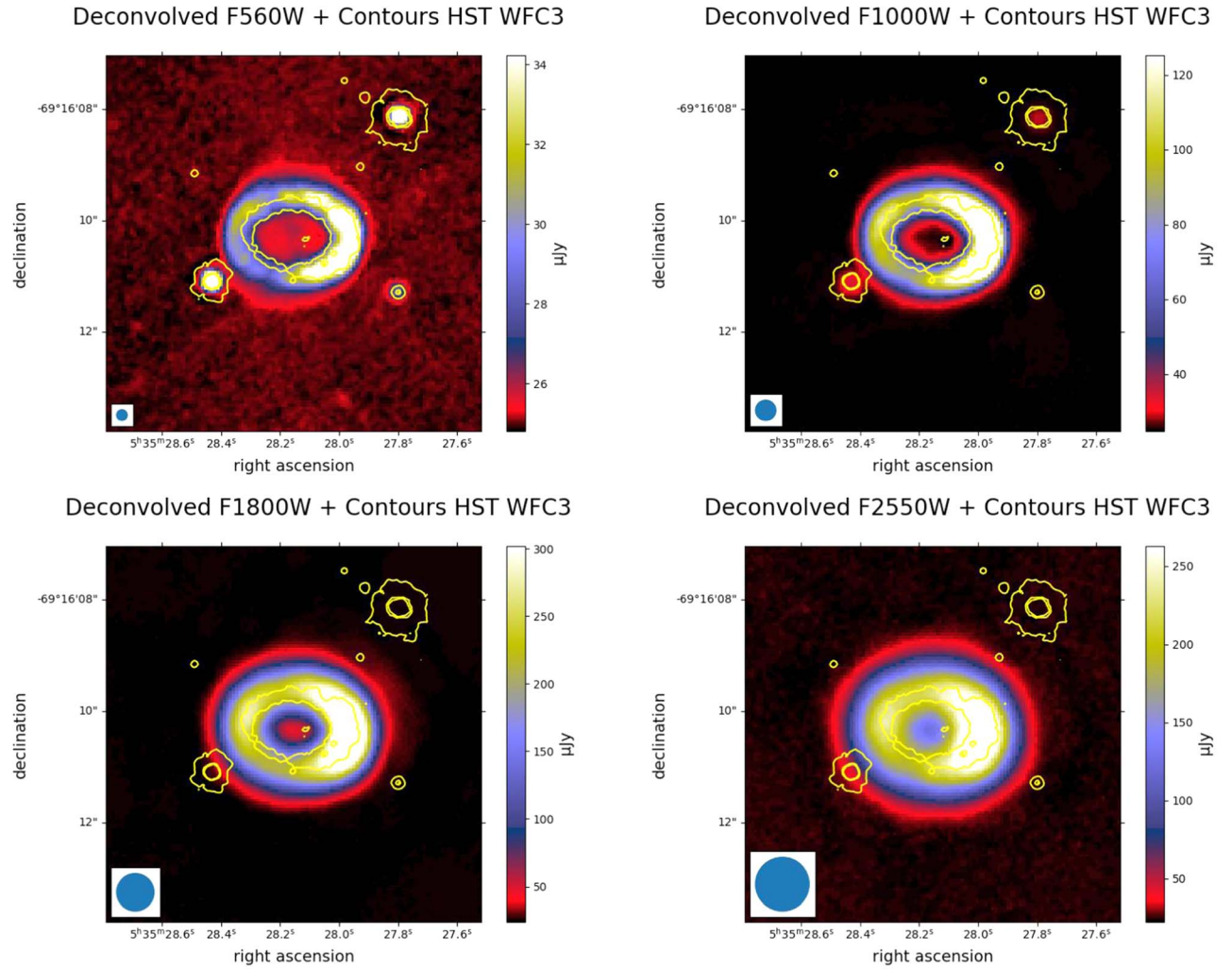


Figure 16. Deconvolved images by CLEAN method at 5.6, 10, 18, and 25.5 μ using Web PSF as dirty beams and the corresponding clean beam (2D Gaussian fit; FWHM Gaussian fit of the actual PSF for each wavelength are on lower left in each panel). Superimposed contours are based on the HST WCF3 image at $\lambda = 0.502 \mu\text{m}$. Most of the extensions around the ER are removed by deconvolution. Contours levels: [0.06, 0.6, 1 electrons s^{-1}].

rings in specific emission lines but not in dust continuum emission. We would therefore expect the NIRCam images reported by Arendt et al. (2023) showing the outer rings to be those dominated by line emission. Of the eight filter images shown in Figure 1 of Arendt et al. (2023), two show the outer rings: the F164N ([Fe II]+[Si I]); and F405N (Br-alpha) images.

5. Summary and Conclusions

Our main results can be summarized as follows:

1. We have obtained MIRI images of SN 1987A taken with four different filters: F560W, F1000W, F1800W, and F2550W, each covering a $56''3 \times 56''3$ field of view. The images are dominated by the bright $\sim 2''$ diameter ER at their center but show extended nebulousity toward the edges of the field, around a cavity with an angular diameter of $\sim 30''$ that surrounds SN 1987A.
2. Thermal dust emission dominates the observed filter in-band fluxes. A comparison of the filter profiles with the MIRI-MRS 5–28 μm spectrum of the ER presented by Jones et al. (2023) shows that line emission makes only a small contribution to the total flux seen in each filter

(ranging from $\lesssim 0.1\%$ up to 2.9%, depending on the filter). Excellent agreement was found between the integrated fluxes measured for the ER with each filter and the equivalent MRS photometric fluxes.

3. Spatial dust temperature and mass maps were constructed for the region encompassing the ER. Using a silicate and amorphous carbon model fit the data from all four filters, dust temperatures vary from 120 to 165 K and masses from 0.2 to $1.5 \cdot 10^{-8} M_{\odot} \text{pixel}^{-1}$, while a fit using the astro dust mixture of Hensley & Draine (2023) led to slightly higher dust temperatures and masses from 0.5 to $3.5 \cdot 10^{-8} M_{\odot} \text{pixel}^{-1}$. The total mass is $1.3 \cdot 10^{-5} M_{\odot}$ and $2.8 \cdot 10^{-5} M_{\odot}$, respectively. The total mass is 10 times greater than the mass reported in 2006 (Bouchet et al. 2006). A fit with the astro dust model to just the 18–25.5 μm image ratio led to lower dust temperatures of between 105 and 140 K.
4. No evidence for an unresolved compact object was found in any of our four continuum-dominated images.
5. We searched for evidence for extended emission beyond the “knotty” ER seen at shorter wavelengths—however, most of the apparent extensions around the ER seen in our MIRI images appear to arise from PSF effects and

were removed by deconvolution with the CLEAN algorithm.

The most striking fact is that in our temperature maps the inner ring (ER) is not well defined. The IR emission in the temperature maps extends well beyond the ER, which is difficult to visualize in our direct images. The other highlight is that the IR emission from the east side of the ring is quite a bit fainter at these mid-IR wavelengths than that from the west side. This seems to be an indication that dust has been disrupted in the east region. On both sides, we may see remains of silicates. This suggests that it is now difficult to use conventional models to model the IR emission in and outside the ER. Although this is a hazardous and very speculative hypothesis, we suggest that the emission from beyond the ER may be synchrotron or another emission mechanism (ongoing work).

Acknowledgments

This work is based on observations made with the NASA/ESA/CSA James Webb Space Telescope. Some/all of the data presented in this article were obtained from the Mikulski Archive for Space Telescopes (MAST) at the Space Telescope Science Institute, which is operated by the Association of Universities for Research in Astronomy, Inc., under NASA contract NAS 5-03127 for JWST. The specific observations analyzed can be accessed via DOI:10.17909/k6j3-vm72. These observations are associated with program #1232. L.L. acknowledges support from the NSF through grant 2054178. OCJ acknowledges support from an STFC Webb fellowship. C.N. acknowledges the support of an STFC studentship. M.M. and N.H. acknowledge that a portion of their research was carried out at the Jet Propulsion Laboratory, California Institute of Technology, under a contract with the National Aeronautics and Space Administration (80NM0018D0004). M.M. and N.H. acknowledge support through NASA/JWST grant 80NSSC22K0025. P.J.K. and J.J. acknowledge support from the Science Foundation Ireland/Irish Research Council Pathway program under grant No. 21/PATH-S/9360. M.J.B. acknowledges support from the European Research Council Advanced Grant 694520 SNDUST. O.N. acknowledges the NASA Postdoctoral Program at NASA Goddard Space Flight Center, administered by Oak Ridge Associated Universities under contract with NASA. A.S.H. is supported in part by an STScI Postdoctoral Fellowship. L.C. acknowledges support by grant PIB2021-127718NB-100, from the Spanish Ministry of Science and Innovation/State Agency of Research MCIN/AEI/10.13039/50110001103. C.F. and J.L. acknowledge support from the Swedish Space Agency. T.T. acknowledges financial support from the UK Science and Technology Facilities Council and the UK Space Agency. J.B. and B.V. thank the Belgian Federal Science Policy Office (BELSPO) for the provision of financial support in the framework of the PRODEX Programme of the European Space Agency (ESA). Finally, we thank the referee for the comments and constructive advice.

Facility: JWST (MIRI)

Software: Astropy (Astropy Collaboration et al. 2022), Matplotlib (Hunter 2007), PyPHER Boucaud et al. (2016), GDL (Park et al. 2022), MPFIT (Markwardt 2009).

Appendix Reduction Method

We did not follow the architecture of the official pipeline²⁹ for the following reasons:

1. Not all the configuration files were up to date, and the pipeline was not fully tested at the time of our analysis.
2. We were mainly interested in a small region around the center (40 pixels wide), encompassing the ER and the outer rings. Note that in our dedicated pipeline, we only used three calibration files for (i) the nonlinearity correction, (ii) the mask for the dead and hot pixels, and (iii) the photometric conversion to Janskys. The dark correction was included in the correction of the background. The flat field correction was small because the region of interest is small and in the center of the image. The mosaicking took care of that correction.

We thus proceeded as follows:

1. We applied a nonlinearity correction (see Figure 17). The ramps were then transformed into slopes (linear regression with deglitching of the official pipeline), and we computed the median of consecutive differences (see Figure 18).
2. We computed the differences between two sequential consecutive frames. Outliers were thus flagged (deglitching), and the first and the two penultimate frames were disregarded.
3. We computed the background outside of the region of interest and interpolated it on the overall image to be subtracted. This allowed the (weak) dark current to be taken into account and to correct for the odd-even row effect (Figure 19).
4. We used the median of the sequential consecutive differences to compute the slopes.
5. We merged the different dithered pointings for each filter.
6. We then calibrated the data in Jansky pixel^{-1} units.
7. We use the WCS alignment tool JHAT (Rest et al. 2023) to align the F560W and F1000W images to Gaia DR2, with a scatter of about 0.1 pixels. In addition, the F1000W shows a small systematic bias of about 0.2 pixels across the full detector. The longer wavelength images do not have enough stars to do a reliable WCS

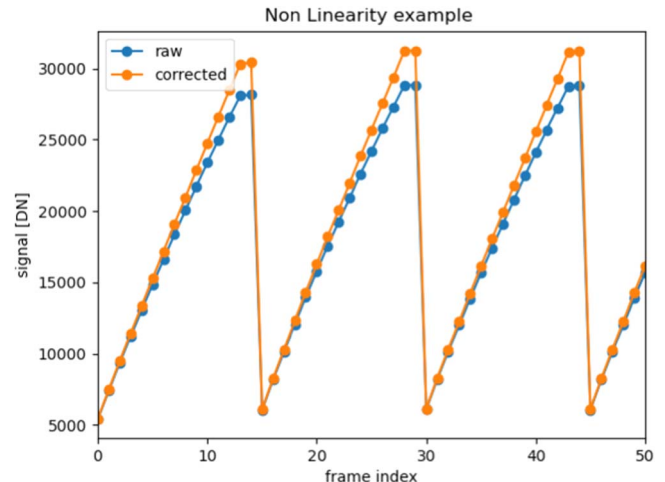


Figure 17. Raw data sample ramps, before and after nonlinearity correction.

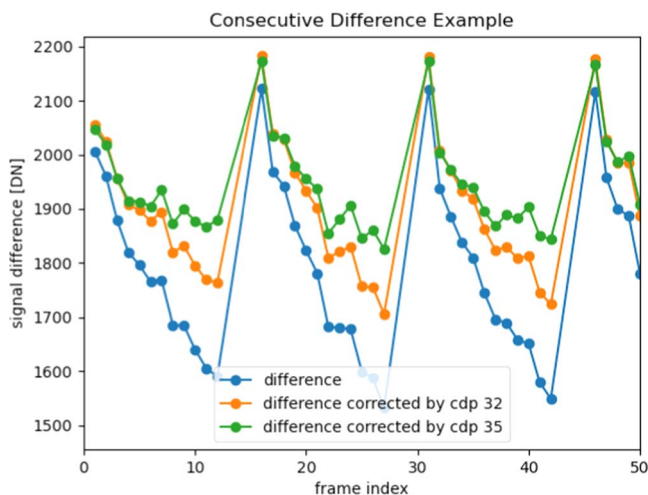


Figure 18. Differences of two consecutive frames, with and without linearity correction. With a perfect correction, the differences should be constant, which is clearly not the case. However, there is a periodic pattern which clearly shows that it can be improved.

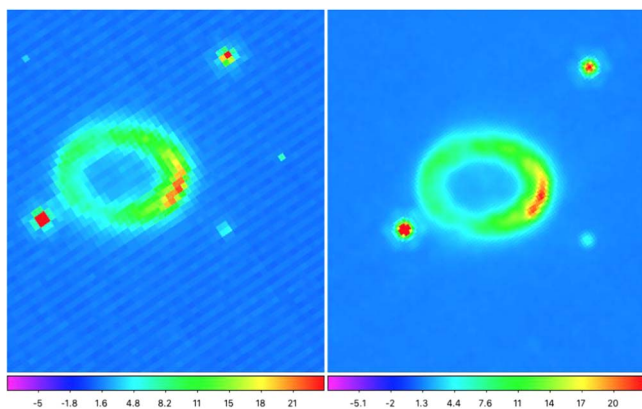


Figure 19. Background subtraction for the 5.6 μm filter, odd/even effect correction: without correction (left panel), with correction (right panel).

alignment, and we therefore propagate the WCS solution from F560W and F1000W to F1800W and F2550W. The next step was to check the astrometry with companion stars 2 and 3, seen at 5.6 μm and marginally at 10 μm . In the dithering mode, the official pipeline gives relative xoffset and yoffset and absolute WCS values. These values are half-integers, so we had to re-bin by a factor of 2 (centering and mean). Note, for example, that comparing filters F560W and F1000W, we see a one-pixel shift, which is most probably due to the fact that different filters introduce slight deflections of the beam.

ORCID iDs

P. Bouchet <https://orcid.org/0000-0002-6018-3393>
 R. Gastaud <https://orcid.org/0009-0007-5200-1362>
 A. Coulais <https://orcid.org/0000-0001-6492-7719>
 M. J. Barlow <https://orcid.org/0000-0002-3875-1171>
 C. Fransson <https://orcid.org/0000-0001-8532-3594>
 P. J. Kavanagh <https://orcid.org/0000-0001-6872-2358>

J. Larsson <https://orcid.org/0000-0003-0065-2933>
 T. Temim <https://orcid.org/0000-0001-7380-3144>
 O. C. Jones <https://orcid.org/0000-0003-4870-5547>
 A. S. Hirschauer <https://orcid.org/0000-0002-2954-8622>
 T. Tikkanen <https://orcid.org/0009-0003-6128-2347>
 J. A. D. L. Blommaert <https://orcid.org/0000-0002-5797-2439>
 O. D. Fox <https://orcid.org/0000-0003-2238-1572>
 A. Glasse <https://orcid.org/0000-0002-2041-2462>
 N. Habel <https://orcid.org/0000-0002-2667-1676>
 J. Hjorth <https://orcid.org/0000-0002-4571-2306>
 J. Jaspers <https://orcid.org/0000-0002-0577-1950>
 R. M. Lau <https://orcid.org/0000-0003-0778-0321>
 L. Lenkić <https://orcid.org/0000-0003-4023-8657>
 M. Meixner <https://orcid.org/0000-0002-0522-3743>
 O. Nayak <https://orcid.org/0000-0001-6576-6339>
 A. Rest <https://orcid.org/0000-0002-4410-5387>
 B. Sargent <https://orcid.org/0000-0001-9855-8261>
 R. Wesson <https://orcid.org/0000-0002-4000-4394>
 G. S. Wright <https://orcid.org/0000-0001-7416-7936>
 L. Colina <https://orcid.org/0000-0002-9090-4227>
 E. F. van Dishoeck <https://orcid.org/0000-0001-7591-1907>
 M. Güdel <https://orcid.org/0000-0001-9818-0588>
 Th. Henning <https://orcid.org/0000-0002-1493-300X>
 G. Östlin <https://orcid.org/0000-0002-3005-1349>
 T. P. Ray <https://orcid.org/0000-0002-2110-1068>
 B. Vandenbussche <https://orcid.org/0000-0002-1368-3109>

References

- Alekseev, E. N., Alekseeva, L. N., Volchenko, V. I., & Krivosheina, I. V. 1987, *JETPL*, **45**, 589
- Alp, D., Larsson, J., Fransson, C., et al. 2018, *ApJ*, **864**, 174
- Alp, D., Larsson, J., & Fransson, C. 2021, *ApJ*, **916**, 76
- Arendt, R. G., Boyer, M. L., Dwek, E., et al. 2023, *ApJ*, **959**, 12p
- Arendt, R. G., Dwek, E., Bouchet, P., et al. 2016, *AJ*, **151**, 62
- Arendt, R. G., Dwek, E., Bouchet, P., et al. 2020, *ApJ*, **890**, 2
- Argyriou, I., Glasse, A., Law, D. R., et al. 2023, *A&A*, **675**, A111
- Astropy Collaboration, Price-Whelan, A. M., Lim, P. L., et al. 2022, *ApJ*, **935**, 167
- Bionta, R. M., Blewitt, G., Bratton, C. B., et al. 1987, *PhRvL*, **58**, 1494
- Borkowski, K. J., Blondin, J. M., & McCray, R. 1997, *ApJ*, **477**, 281
- Boucaud, A., Bocchio, M., Abergel, A., et al. 2016, *A&A*, **596**, A63
- Bouchet, P., & Danziger, J. 2014, in *IAU Symp. 296, Supernova Environmental Impacts*, ed. A. Ray & R. A. McCray (Cambridge: Cambridge Univ. Press), 9
- Bouchet, P., De Buizer, J. M., Suntzeff, N. B., et al. 2004, *ApJ*, **611**, 394
- Bouchet, P., Dwek, E., Danziger, J., et al. 2006, *ApJ*, **650**, 212
- Bouchet, P., García-Marín, M., Lagage, P. O., et al. 2015, *PASP*, **127**, 612
- Burrows, A. 1988, *ApJ*, **334**, 891
- Burrows, C. J., Krist, J., Hester, J. J., et al. 1995, *ApJ*, **452**, 680
- Cendes, Y., Gaensler, B. M., Ng, C. Y., et al. 2018, *ApJ*, **867**, 65
- Chevalier, R. A., & Dwarkadas, V. V. 1995, *ApJL*, **452**, L45
- Cigan, P., Matsuura, M., Gomez, H. L., et al. 2019, *ApJ*, **886**, 51
- Draine, B. T., & Lee, H. M. 1984, *ApJ*, **285**, 89
- Dwek, E., Arendt, R. G., Bouchet, P., et al. 2008, *ApJ*, **676**, 1029
- Dwek, E., Arendt, R. G., Bouchet, P., et al. 2010, *ApJ*, **722**, 425
- Frank, K. A., Zhekov, S. A., Park, S., et al. 2016, *ApJ*, **829**, 40
- Fransson, C., Barlow, M., Kavanagh, P. J., et al. 2024, *Sci*, **383**, 898
- Fransson, C., Larsson, J., Migotto, K., et al. 2015, *ApJL*, **806**, L19
- Gaensler, B. M., Manchester, R. N., Staveley-Smith, L., et al. 1997, *ApJ*, **479**, 845
- Gardner, J. P., Mather, J. C., Abbott, R., et al. 2023, *PASP*, **135**, 068001
- Gilmozzi, R., Cassatella, A., Clavel, J., et al. 1987, *Natur*, **328**, 318
- Hashimoto, M., Nomoto, K., & Shigeyama, T. 1989, *A&A*, **210**, L5
- Helder, E. A., Broos, P. S., Dewey, D., et al. 2013, *ApJ*, **764**, 11
- Hensley, B. S., & Draine, B. T. 2023, *ApJ*, **948**, 959
- Hildebrand, R. H. 1983, *QJRAS*, **24**, 267

²⁹ <https://jwst-docs.stsci.edu/jwst-science-calibration-pipeline-overview>

- Hirata, K., Kajita, T., Koshiba, M., et al. 1987, in *Neutrino Masses and Neutrino Astrophysics (Including Supernova 1987a)*, ed. V. Barger et al., 51
- Högbom, J. A. 1974, *A&AS*, 15, 417
- Hunter, J. D. 2007, *CSE*, 9, 90
- Indebetouw, R., Matsuura, M., Dwek, E., et al. 2014, *ApJL*, 782, L2
- Jones, O. C., Kavanagh, P. J., Barlow, M. J., et al. 2023, *ApJ*, 958, 95
- Kirshner, R. P., Sonneborn, G., Crenshaw, D. M., & Nassiopoulos, G. E. 1987, *ApJ*, 320, 602
- Larsson, J., Fransson, C., Alp, D., et al. 2019, *ApJ*, 886, 147
- Larsson, J., Fransson, C., Östlin, G., et al. 2011, *Natur*, 474, 484
- Larsson, J., Fransson, C., Sargent, B., et al. 2023, *ApJL*, 949, L27
- Larsson, J., Sollerman, J., Lyman, J. D., et al. 2021, *ApJ*, 922, 265
- Lawrence, S. S., Sugerman, B. E., Bouchet, P., et al. 2000, *ApJL*, 537, L123
- Maitra, C., Haberl, F., Sasaki, M., et al. 2022, *A&A*, 661, A30
- Manchester, R. N. 2007, in *AIP Conf. Ser. 937, Supernova 1987A: 20 Years After: Supernovae and Gamma-Ray Bursters*, ed. S. Immler, K. Weiler, & R. McCray (Melville, NY: AIP), 134
- Markwardt, C. B. 2009, in *ASP Conf. Ser. 411, Astronomical Data Analysis Software and Systems XVIII*, ed. D. A. Bohlender, D. Durand, & P. Dowler (San Francisco, CA: ASP), 251
- Matsuura, M., Dwek, E., Barlow, M. J., et al. 2015, *ApJ*, 800, 50
- McCray, R. 1993, *ARA&A*, 31, 175
- McCray, R., & Fransson, C. 2016, *ARA&A*, 54, 19
- Panagia, N., Gilmozzi, R., Macchetto, F., Adorf, H. M., & Kirshner, R. P. 1991, *ApJ*, 380, L23
- Park, J., Duvert, G., Coulais, A., et al. 2022, *JOSS*, 7, 4633
- Pun, C. S. J., Kirshner, R. P., Garnavich, P. M., & Challis, P. 1997, *AAS Meeting*, 191, 01
- Ressler, M. E., Sukhatme, K. G., Franklin, B. R., et al. 2015, *PASP*, 127, 675
- Rest, A., Pierel, J., Correnti, M., et al. 2023, *The JWST HST Alignment Tool (JHAT)*, v2, Zenodo, doi:10.5281/zenodo.7892935
- Rosu, S., Larsson, J., Fransson, C., et al. 2024, arXiv:2403.14361
- Smartt, S. J., Eldridge, J. J., Crockett, R. M., & Maund, J. R. 2009, *MNRAS*, 395, 1409
- Sugerman, B. E. K., Crofts, A. P. S., Kunkel, W. E., Heathcote, S. R., & Lawrence, S. S. 2005, *ApJS*, 159, 60
- Sukhbold, T., Ertl, T., Woosley, S. E., Brown, J. M., & Janka, H. T. 2016, *ApJ*, 821, 38
- West, R. M., Madsen, C., Bahcall, J., et al. 1987, *IAU Circ.*, 4329, 2
- White, G. L., & Malin, D. 1987, in *ESO Workshop on the SN*, ed. I. J. Danziger (Garching: ESO), 11
- Woosley, S. E. 1988, *ApJ*, 330, 218
- Woosley, S. E., Pinto, P. A., Martin, P. G., & Weaver, T. A. 1987, *ApJ*, 318, 664
- Zanardo, G., Staveley-Smith, L., Gaensler, B. M., et al. 2018, *ApJL*, 861, L9
- Zhang, S. B., Dai, S., Hobbs, G., et al. 2018, *MNRAS*, 479, 1836